

Article

High Throughput Preparation of Ag-Zn Alloy Thin Films for the Electrocatalytic Reduction of CO₂ to CO

Jiameng Sun¹, Bin Yu¹, Xuejiao Yan², Jianfeng Wang¹, Fuquan Tan¹, Wanfeng Yang¹, Guanhua Cheng^{1,*} and Zhonghua Zhang^{1,*}

¹ Key Laboratory for Liquid-Solid Structural Evolution and Processing of Materials (Ministry of Education), School of Materials Science and Engineering, Shandong University, Jinan 250061, China

² Taian Institute of Supervision & Inspection on Product Quality, Taian 271000, China

* Correspondence: guanhua.cheng@sdu.edu.cn (G.C.); zh_zhang@sdu.edu.cn (Z.Z.)

Abstract: Ag-Zn alloys are identified as highly active and selective electrocatalysts for CO₂ reduction reaction (CO₂RR), while how the phase composition of the alloy affects the catalytic performances has not been systematically studied yet. In this study, we fabricated a series of Ag-Zn alloy catalysts by magnetron co-sputtering and further explored their activity and selectivity towards CO₂ electroreduction in an aqueous KHCO₃ electrolyte. The different Ag-Zn alloys involve one or more phases of Ag, AgZn, Ag₅Zn₈, AgZn₃, and Zn. For all the catalysts, CO is the main product, likely due to the weak CO binding energy on the catalyst surface. The Ag₅Zn₈ and AgZn₃ catalysts show a higher CO selectivity than that of pure Zn due to the synergistic effect of Ag and Zn, while the pure Ag catalyst exhibits the highest CO selectivity. Zn alloying improves the catalytic activity and reaction kinetics of CO₂RR, and the AgZn₃ catalyst shows the highest apparent electrocatalytic activity. This work found that the activity and selectivity of CO₂RR are highly dependent on the element concentrations and phase compositions, which is inspiring to explore Ag-Zn alloy catalysts with promising CO₂RR properties.



Citation: Sun, J.; Yu, B.; Yan, X.; Wang, J.; Tan, F.; Yang, W.; Cheng, G.; Zhang, Z. High Throughput Preparation of Ag-Zn Alloy Thin Films for the Electrocatalytic Reduction of CO₂ to CO. *Materials* **2022**, *15*, 6892. <https://doi.org/10.3390/ma15196892>

Academic Editor: Ilya V. Mishakov

Received: 3 September 2022

Accepted: 30 September 2022

Published: 4 October 2022

Publisher's Note: MDPI stays neutral with regard to jurisdictional claims in published maps and institutional affiliations.



Copyright: © 2022 by the authors. Licensee MDPI, Basel, Switzerland. This article is an open access article distributed under the terms and conditions of the Creative Commons Attribution (CC BY) license (<https://creativecommons.org/licenses/by/4.0/>).

Keywords: high throughput; electrocatalysis; CO₂ reduction; magnetron sputtering; silver-zinc alloy

1. Introduction

With the worldwide consumption of fossil fuels, the increasing emission of carbon dioxide (CO₂) in the atmosphere is becoming a more and more serious environmental threat [1–3]. Artificial conversion of CO₂ into fuels and chemical feedstocks is essential to reduce the concentration of CO₂ and mitigate the greenhouse effect. The available methods include electrochemical, photoelectrochemical, thermochemical, and biological conversions, of which electrochemical reduction is regarded as a clean and effective method due to its mild reaction conditions and ability to use renewable electricity [4–6].

Electrochemical CO₂ reduction reaction (CO₂RR) can yield a variety of products through two-, four-, six-, and eight-electron pathways, such as carbon monoxide (CO), methane (CH₄), formic acid (HCOOH), methanol (CH₃OH) and C₂/C₃ compounds [3,7–9]. CO is the simplest and one of the most common products of CO₂RR due to the sluggish kinetics of C–C coupling, which can be further electrocatalytically reduced to high-value chemicals or used as a component of syngas to produce hydrocarbon fuels (e.g., aldehydes, methanol, and phosgene) by the Fischer-Tropsch process [10,11]. Therefore, it is important to study efficient catalysts to selectively reduce CO₂ to CO (CO₂+2H⁺+2e[−] ↔ CO + H₂O) [12]. However, the first step of CO₂RR requires a larger overpotential compared to hydrogen evolution reaction (HER: 2H⁺+2e[−] ↔ H₂), which will inevitably occur as a main competitive reaction in the aqueous CO₂ reduction system [13,14]. The challenges of CO₂RR are the high overpotential, kinetically sluggish multi-electron transfer process, and the selectivity against the HER. Developing promising CO₂RR catalysts with high activity and selectivity will be the key point to efficiently utilizing CO₂.

Various metals (e.g., Au, Ag, Zn) have been identified as potential electrocatalysts to overcome the sluggish kinetics of CO₂ activation and improve the selectivity of CO [12,15,16]. The Sabatier principle shows that adsorbed CO (CO*) is an important reaction intermediate for the production of hydrocarbons and oxygen-containing compounds, and optimal binding energy of CO* ($E_B[\text{CO}]$) can reduce the yield of other products and lead to higher selectivity of CO [17]. Au and Ag show a high selectivity of CO in CO₂RR, due to the low HER activity and weak $E_B[\text{CO}]$ [18]. Ag is a more cost-effective catalyst for selective reduction of CO₂ to CO compared to Au, which is more than 70 times more expensive than Ag [19]. Zn possesses the ability to form CO in CO₂RR, which is an earth-abundant metal and much cheaper than Ag. Although Zn does not show satisfying activity and selectivity, it is one of the most promising non-previous metals for CO₂RR in the CO-forming class [20]. Jaramillo and Nørskov et al. reported that the binding energy of adsorbed COOH (COOH*, $E_B[\text{COOH}]$) is a key descriptor for CO generation efficiency in the CO₂RR [21]. In the volcano plot of $E_B[\text{COOH}]$, Ag and Zn appear on the weak- and strong-binding legs of the plot respectively [12], therefore, Ag-Zn alloys would have a more appropriate $E_B[\text{COOH}]$ to improve the activity of CO₂RR than either single metal (Ag or Zn) [12]. Taking advantage of the synergistic effect, Ag-Zn alloys may be able to increase the CO selectivity and activity of CO₂RR while reducing the catalyst cost.

High-throughput catalyst screening technique is a promising scientific method, which has been developed for the discovery and optimization of catalysts. Using this method can speed up the catalyst discovery process in exploring the complex catalyst composition space, such as alloying elements and surface molecules [22,23]. Applying the concept of high throughput in material preparation, samples with different element concentrations can be prepared directly at one time, significantly simplifying the sample preparation process, and providing convenience for the subsequent exploration of electrochemical properties.

In this work, to identify the relation between the CO₂RR activity and the element concentrations as well as phase compositions of Ag-Zn alloys, we applied the concept of high throughput in material preparation and synthesized a series of Ag-Zn bimetallic alloys by composition gradient sputtering. The selectivity and activity of the CO₂RR on catalysts with different element concentrations and phase compositions were compared for the efficient electrochemical production of CO.

2. Experimental

2.1. Catalysts Preparation

The Ag-Zn alloy catalysts were prepared by magnetron sputtering using carbon fiber paper (CFP) as the substrate. CFP was ultrasonically cleaned in ethanol for 5 min and dried at 60 °C in air. Subsequently, Ag and Zn were directly deposited onto the CFP using direct-current magnetron sputtering equipment (SKY Technology Development Co., Ltd., Shenyang, China) with a working distance of 6 cm. High-purity Ag and Zn (99.99 wt.%, Beijing Dream Material Technology Co., Ltd., Beijing, China) were used as the sputtering targets. The normal inclination angle between the target and CFP substrate was 20°, and the sample holder stood still to obtain samples with concentration gradients [24,25]. The sputtering was operated at room temperature for 1 h, with a power of 25 W for the Ag target and 35 W for the Zn target, and an Ar pressure of 1 Pa at a flow rate of 30 cm³ min⁻¹. Similarly, pure Ag and Zn were also sputtered on CFP, respectively. The sputtering power was 25 W for Ag and 35 W for Zn at a rotating speed of 5 revolutions per minute for the substrate. Finally, we obtained uniform Ag and Zn films with a mass loading of around 0.7 mg cm⁻², and Ag-Zn alloy films with different concentrations and a mass loading of about 1.4 mg cm⁻².

2.2. Material Characterizations

X-ray diffraction (XRD) patterns were recorded by an XD-3 diffractometer equipped with Cu K α radiation (Beijing Purkinje General Instrument Co., Ltd., Beijing, China). The microstructures and chemical compositions of the samples were characterized by a

scanning electron microscope (SEM, COXEM EM-30, Daejeon, Korea) equipped with an energy dispersive X-ray (EDX) analyzer.

2.3. Electrochemical Measurements

Electrochemical measurements were conducted on a CHI 760E potentiostat in an H-type cell with an ion-exchange membrane separator (Nafion 117 membrane, FuelCell Store, TX, America) inserted between the cathodic and anodic chambers. 0.5 M KHCO₃ solution was used as the electrolyte in both the cathode and anode compartments. The sputtering samples, a Pt foil, and a double-junction saturated calomel electrode (SCE, saturated KCl, TIANJINAIDA R0232, Tianjin, China) were used as the working, counter, and reference electrodes, respectively. The potentials reported in this work were converted to be against the reversible hydrogen electrode (RHE) according to the following equation:

$$E_{\text{RHE}} = E_{\text{SCE}} + 0.241 + 0.059 \times \text{PH} \quad (1)$$

A chronoamperometric electrolysis test was carried out at the working electrode with a geometric area of 1 cm². Before the test, the fresh electrolyte solution was bubbled with high-purity CO₂ for 15 min, and the test was under a continuous CO₂ (99.9%) gas flow of 20 mL min⁻¹. The gas-phase products from the gastight cathodic compartment were directly introduced into a gas chromatograph (GC, Lunan Instrument GC-7820, Jinan, China) which used high-purity Ar as the carrier gas for all compartments and analyzed using a thermal conductivity detector (TCD) and two flame ionization detectors (FID1 and FID2). The amount of CO gas was estimated from the FID1 data and H₂ gas from the TCD data. An external standard method was adopted to quantify the products. The gas-phase products were injected into GC every 12 min during the CO₂RR in the chronoamperometry measurement mode.

3. Results and Discussion

3.1. Preparation and Characterization of the Ag-Zn Alloys as well as Pure Ag, Zn Films

As illustrated in Figure 1a, the Ag-Zn alloy film was sputtered on CFP by a co-sputtering method. The macroscopic picture of the sputtering film in Figure 1b, shows a color gradient, indicating a corresponding concentration gradient in different regions. The sample appears black gray and bright silver on the side near the Zn target and the Ag target, respectively, and shows a color transition between the two regions. The concentration gradient distribution of the obtained Ag-Zn alloy film is shown in Figure 1c,d based on EDX analysis, and several respective results (e.g., Ag₁₀Zn₉₀, Ag₂₀Zn₈₀, Ag₃₀Zn₇₀, Ag₃₅Zn₆₅, Ag₄₀Zn₆₀, Ag₄₅Zn₅₅, Ag₅₅Zn₄₅, Ag₇₀Zn₃₀, and Ag₈₅Zn₁₅) are shown in Figure S1. In addition, pure Ag and Zn films with a uniform composition were prepared by sputtering with the single respective metal target. The macroscopic view of the pure Zn and Ag films shows that the film color is consistent with the respective metal target (Figure S2).

The morphologies and structures of the Ag-Zn alloy films were investigated by SEM. It obviously shows that the surface of pure Zn film is grainy (Figure 2a), while it is smooth and without obvious features for the pure Ag film (Figure 2b). As shown in Figure S3, with the Ag concentration increasing, the roughness of the film surface decreases and becomes smooth gradually. When the atomic percentage of Ag reaches 20%, the film becomes relatively smooth, and a further increase in Ag concentration shows little effect on the morphology. The Ag₄₅Zn₅₅ alloy shows similar surface morphology as that of pure Ag film as shown in Figure 2c. The EDX mappings (Figure 2d–f) show both Ag and Zn coat well on the fiber surface of the CFP.

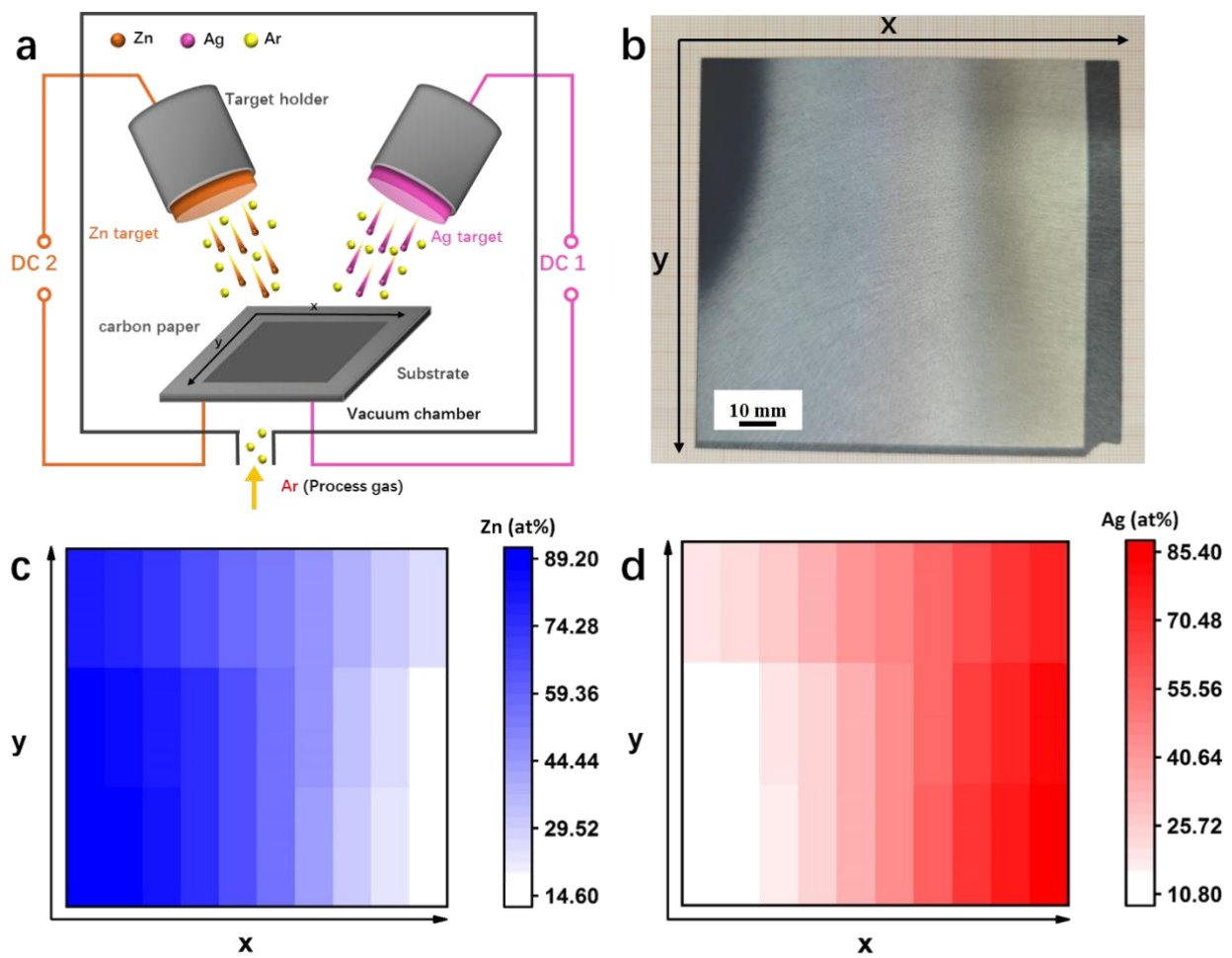


Figure 1. (a) Schematic illustration showing the preparation process of the Ag-Zn film catalysts by co-sputtering. (b) Macroscopic view of the Ag-Zn film after co-sputtering. (c,d) Concentration gradient distribution of (c) Zn and (d) Ag elements.

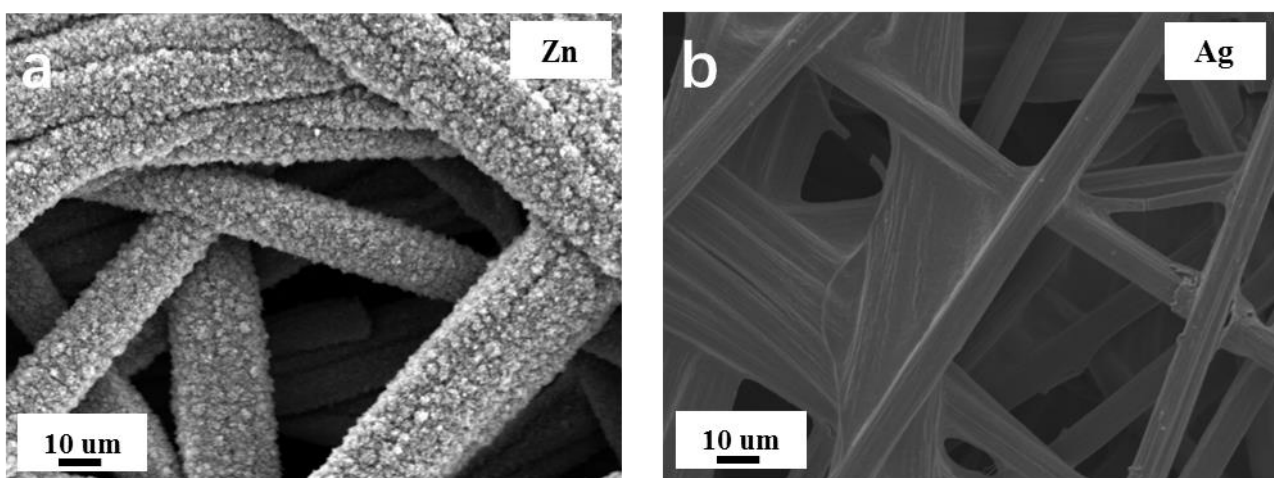


Figure 2. Cont.

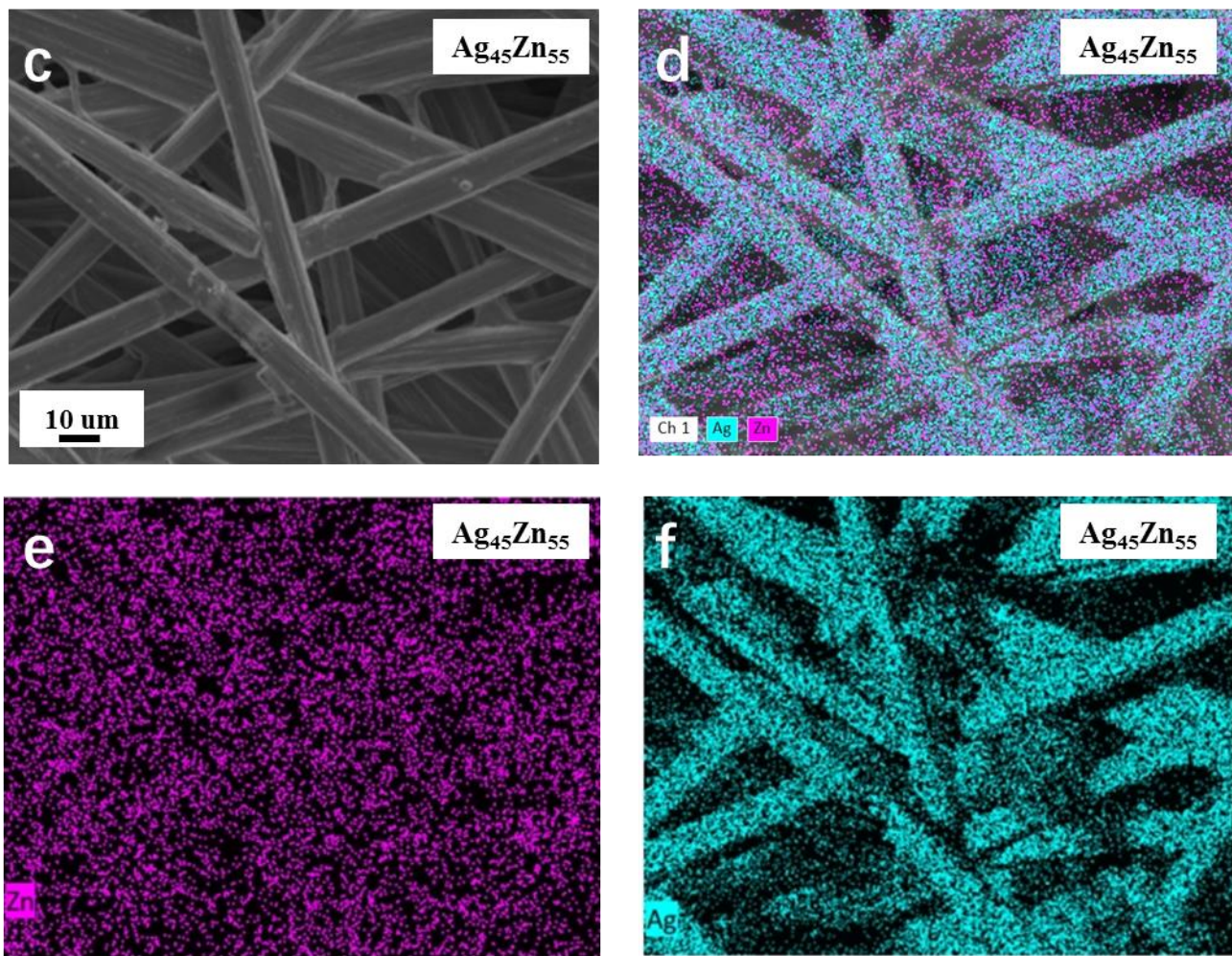


Figure 2. (a–c) SEM images of the (a) Zn, (b) Ag, and (c) $\text{Ag}_{45}\text{Zn}_{55}$ films. (d–f) EDX mapping images of the $\text{Ag}_{45}\text{Zn}_{55}$ film.

The phase constitutions of the selected samples with different concentrations were characterized by XRD in Figure 3a. The characteristic peaks at 18.0° , 26.4° , and 54.5° are ascribed to CFP (Figure S4). The diffraction peaks of pure Ag film at 38.1° , 44.3° , 64.4° , 77.4° , and 81.5° are consistent with the standard Ag phase (PDF #65-2871). For the $\text{Ag}_{55}\text{Zn}_{45}$, $\text{Ag}_{70}\text{Zn}_{30}$, and $\text{Ag}_{85}\text{Zn}_{15}$ catalysts, the diffraction peaks of Ag are observed to shift towards higher 2θ angles, indicating the formation of Ag(Zn) solid solution alloy associated with the lattice distortion/contraction (Figure 3b) [26]. As shown in Figure 3c,d, other catalysts with a smaller atomic ratio of Ag to Zn consist of the AgZn phase ($\text{Ag}_{45}\text{Zn}_{55}$, $\text{Ag}_{40}\text{Zn}_{60}$, and $\text{Ag}_{35}\text{Zn}_{65}$), Ag_5Zn_8 phase ($\text{Ag}_{30}\text{Zn}_{70}$ and $\text{Ag}_{20}\text{Zn}_{80}$), AgZn_3 phase ($\text{Ag}_{10}\text{Zn}_{90}$) and Zn phase (pure Zn catalyst) according to their diffraction peak positions. Therefore, a series of Ag-Zn alloy films with different compositions and phases were successfully fabricated through the high throughput co-sputtering method.

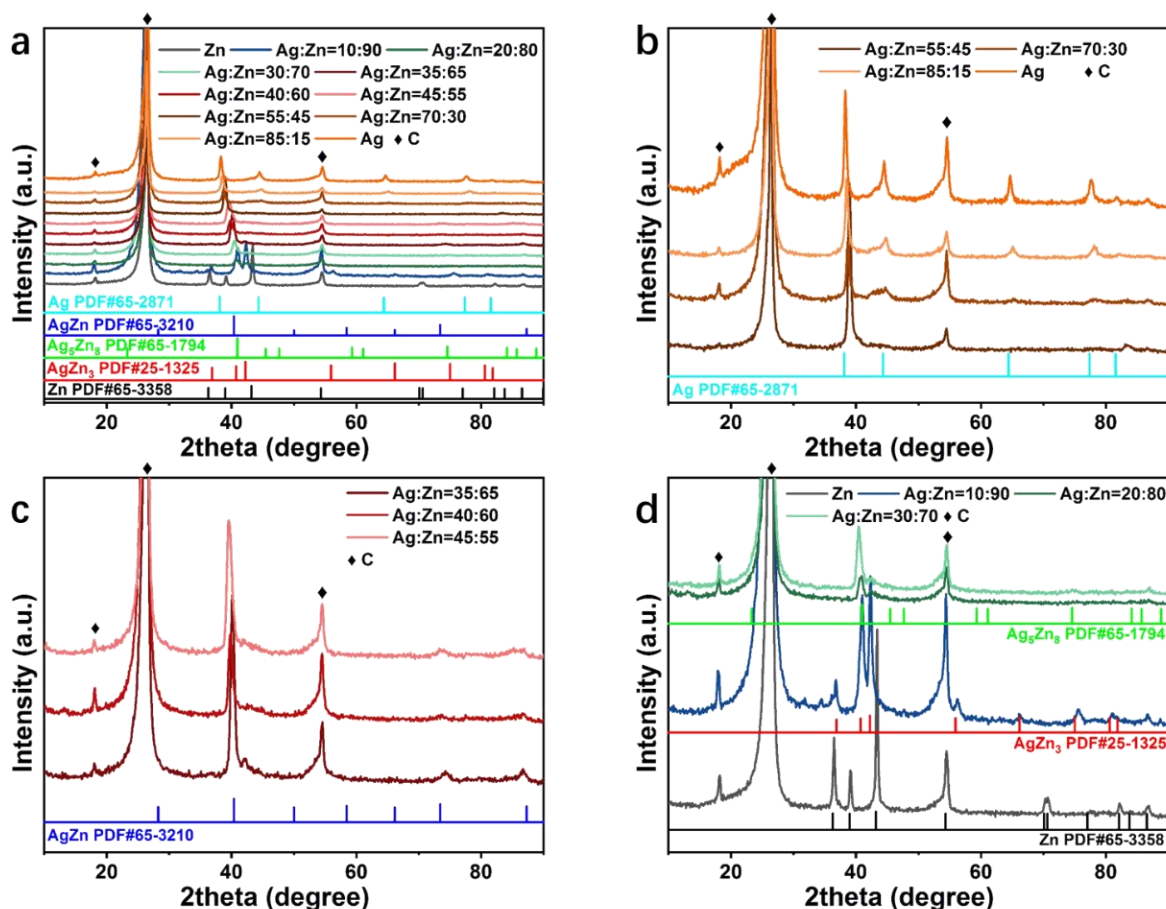


Figure 3. (a) XRD patterns of the pure Zn, pure Ag, and Ag-Zn alloy catalysts with different concentrations. (b–d) XRD patterns of the (b) Ag, Ag₅₅Zn₄₅, Ag₇₀Zn₃₀, Ag₈₅Zn₁₅, (c) Ag₃₅Zn₆₅, Ag₄₀Zn₆₀, Ag₄₅Zn₅₅, and (d) Ag₁₀Zn₉₀, Ag₂₀Zn₈₀, Ag₃₀Zn₇₀, and Zn samples.

3.2. Electrochemical CO₂RR Performance over Ag-Zn Alloys as well as Pure Ag, Zn Films in the H-Cell

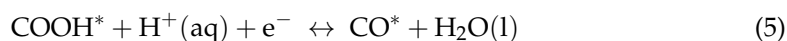
The electrocatalytic performance of CO₂RR was explored over the Ag-Zn alloys in CO₂-saturated 0.5 M KHCO₃ by using a gas-tight H-cell. For comparison, the electrochemical CO₂RR performance of the pure Ag and Zn films was also evaluated under the same reaction conditions. Potentiostatic experiments were conducted at 7 different potentials in the range of −0.6 to −1.2 V vs. RHE. The faradaic efficiency of *x* (FE_{*x*}) production and its partial current density (*j_x*) was calculated as follows [12,27]:

$$FE_x (\%) = \frac{n_x (\text{mol}) \cdot N \cdot F (\text{C mol}^{-1})}{Q (\text{C})} \times 100 = \frac{0.1315 \cdot V \left(\frac{\text{mL}}{\text{min}} \right) \cdot R_x}{1000 \cdot i_{\text{total}} (\text{mA})} \times 100 \quad (2)$$

$$j_x (\text{mA cm}^{-2}) = \frac{i_x (\text{mA})}{A (\text{cm}^2)} = \frac{i_{\text{total}} (\text{mA}) \cdot FE_x}{A (\text{cm}^2)} \quad (3)$$

where *n_x* is the amount of product *x* (mol), *N* is the number of electrons transferred for product *x* formation (*N* is 2 for product CO and H₂), *F* is the Faraday constant (96,485 C mol^{−1}), *Q* is the charge passed to produce *x* (C), *V* is the actual flow rate during the test, *R_x* is the concentration of product *x* from the cathode compartment (obtained from GC data), *i_x* is the current value of product *x* (mA), and *A* is the geometric surface area (cm²). In general, the reduction mechanism of CO₂ to CO is as follows [28]:





where * denotes an active site. A promising catalyst for selectively reducing CO_2 to CO needs to appropriately immobilize COOH^* , therefore, to facilitate the formation of CO^* in the next elementary step (Equation (5)), and to bind CO weakly so that to release the active site easily (Equation (6)). That is, a relatively stronger binding of COOH^* than CO^* is necessary for efficient CO_2RR [17,18].

The faradaic efficiency of CO (FE_{CO}), H_2 (FE_{H_2}) as well as CO and H_2 ($\text{FE}_{\text{CO}\&\text{H}_2}$) of CO_2RR was plotted as a function of applied potentials in Figure 4. CO and H_2 are the major products of the Ag-Zn alloy, indicating that the Ag-Zn alloy is a CO-forming catalyst, akin to Ag and Zn [29]. For all Ag-Zn film electrodes, H_2 is the major product at less negative potentials due to the high overpotential required for CO_2RR [18,30]. Whereas under the moderate potentials, CO is the major product. There is enough electrochemical driving force to reduce CO_2 to CO and sufficient CO_2 supply at the electrode interface so that the reaction rate of CO_2 to CO exceeds that of HER generated from water [31]. At more negative potentials, the mass-transport limitations of CO_2 may suppress CO yielding [18,28].

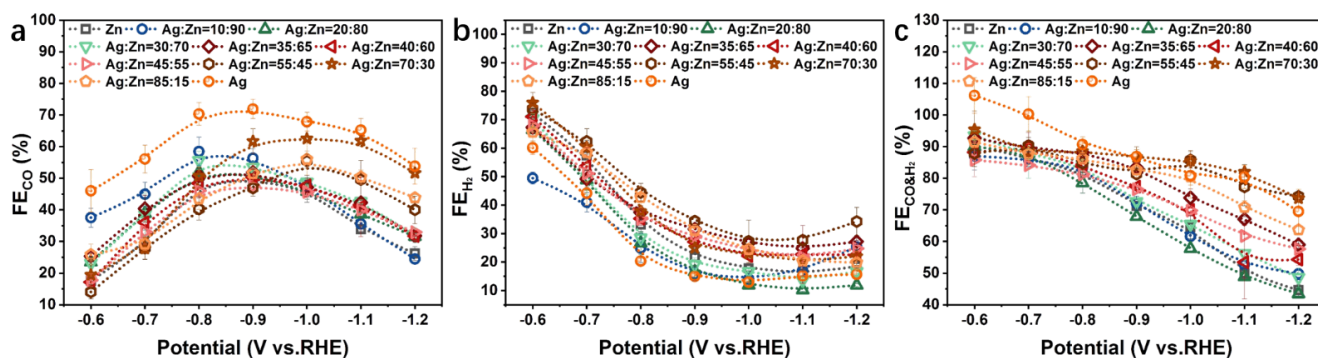


Figure 4. (a) FE_{CO} , (b) FE_{H_2} , and (c) $\text{FE}_{\text{CO}\&\text{H}_2}$ for the pure Zn, pure Ag, and Ag-Zn alloy catalysts with different element concentrations.

As shown in Figure 4a, different phase compositions and concentrations of the Ag-Zn alloy catalysts exhibit different trends of FE_{CO} at $-0.6 \sim -1.2$ V vs. RHE. When the Ag content is high and Ag/Ag(Zn) solid solution phase is displayed, the maximum FE_{CO} appears in the range of $-0.9 \sim -1.0$ V vs. RHE, compared to the range of $-0.8 \sim -0.9$ V vs. RHE for other AgZn and Zn phases. For the Ag(Zn) phase catalysts, pure Ag catalyst shows the highest FE_{CO} over the entire potential range investigated (Figure 4a), and the addition of Zn to Ag decreases CO yielding (Figure S5a), showing that Ag is more effective at reducing CO_2 to CO than the Ag-Zn alloys or Zn. This trend can be explained by the changing of $E_{\text{B}}[\text{CO}]$ [17,28]. The volcano-type relation of the partial current density of CO as a function of $E_{\text{B}}[\text{CO}]$ shows that the catalyst surface with a weak $E_{\text{B}}[\text{CO}]$ can be limited by the activation of CO_2 due to the instability of the COOH^* intermediate, whereas surfaces with a strong $E_{\text{B}}[\text{CO}]$ are limited by highly stabilized CO^* [17]. Both Ag and Zn have weak $E_{\text{B}}[\text{CO}]$ and belong to the category of surfaces limited by the activation of CO_2 . Ag is closer to the top of the volcano plot compared to Zn, and better for CO_2 activation, which explains why Ag is more effective for CO formation [31,32]. When the alloy films consist of the AgZn phase, FE_{CO} decreases with the increase of Ag concentration at the intermediate potentials, while has little change at low and high potentials (Figure S5b). Pure Zn catalyst shows the lowest current efficiency for CO production, and the small amount addition of Ag (10 at.%) significantly improves the FE_{CO} by $\sim 100\%$ at $-0.6 \sim -0.7$ V vs. RHE (Figure S5c). At higher potentials, the AgZn_3 phase catalyst shows the closest FE_{CO} to pure Ag catalyst, but with the potential decreasing, it is consistent with the pure Zn. The CO yielding of the Ag_5Zn_8 catalyst is higher than that of pure Zn and increases with the increase of Ag concentration at lower potentials. This indicates that the AgZn_3 phase

catalyst is favorable for CO production at higher potentials, while the Ag_5Zn_8 phase catalyst is favorable at lower potentials. The scenario of increased CO selectivity of the Ag-Zn alloys compared to Zn at intermediate potentials may originate from the electron transfer from Ag to Zn [33], due to the lower work function of Ag (4.26 eV) than Zn (4.33 eV) [34–36]. The transferred electrons are found to fill the bonding states of localized d-orbitals and exhibit a conspicuous upshift toward the Fermi level, which enhances the adsorption of the intermediate COOH^* , resulting in a higher catalytic activity for CO production compared to pure Zn catalysts [35,37].

Figure 4b shows the changes of FE_{H_2} with potentials, which are basically the same for all Ag-Zn film electrodes. FE_{H_2} decreases rapidly with the potential decreasing, and tends to flatten or even slightly rebound at lower potentials. This indicates that water decomposition is more favorable at less negative potentials, while more active sites are occupied by CO_2 and related intermediates at more negative potentials. Pure Ag, Ag_5Zn_8 ($\text{Ag}_{30}\text{Zn}_{70}$ and $\text{Ag}_{20}\text{Zn}_{80}$ catalysts), AgZn_3 ($\text{Ag}_{10}\text{Zn}_{90}$ catalyst), and pure Zn phase catalysts exhibit lower FE_{H_2} , whereas that of Ag(Zn) solid solution and AgZn phase catalysts is higher (Figure S6), indicating that the former can inhibit HER better.

It can be seen from Figure 4c that the combined faradaic efficiency of CO and H_2 can reach over 80% at the less negative potential range, and almost no other products are produced. This is due to the weak $E_{\text{B}}[\text{CO}]$ at lower overpotential, leading to the rapid desorption of CO from the surface once generated, and therefore, it is difficult to carry out further reduction [31]. In addition, other complex products require multiple proton-electron transfer steps and a larger driving force (more negative potentials) [18]. The $\text{FE}_{\text{CO}\&\text{H}_2}$ for Ag/Ag(Zn) solid solution alloy catalysts decreases by 20–30% at a more negative potential (Figure S7a), that of AgZn phase catalysts decreases by about 30% (Figure S7b), and that of Ag_5Zn_8 , AgZn_3 as well as pure Zn phase catalysts decreases by about 40% (Figure S7c). This is ascribed to the formation of other liquid products, demonstrating an unfavorable competition between the further reduction of CO^* and desorption of CO [18,31]. An explanation is that a higher overpotential provides a higher driving force and improves the electron transfer, which enhances CO^* electroreduction, competing with the non-faradaic step of CO desorption [31].

Figure 5a presents the overall electrode activity of the Ag-Zn alloys as well as pure Zn and Ag as a function of the applied potentials. For all electrodes, a well-defined exponential increase in the overall activity is observed with decreasing potentials. With the addition of Zn in Ag, the total current densities (j_{total}) increase for the Ag/Ag(Zn) solid solution phase catalysts at all potentials (Figure S8a). The catalysts with other phases exhibit a similar level of j_{total} , which is higher than that of the pure Ag catalyst (Figure S8b,c). Notably, the AgZn_3 phase catalyst ($\text{Ag}_{10}\text{Zn}_{90}$) exhibits an especially high j_{total} . This indicates that Ag-Zn alloying will improve the activity of the catalysts, and the AgZn_3 phase catalyst has the highest activity.

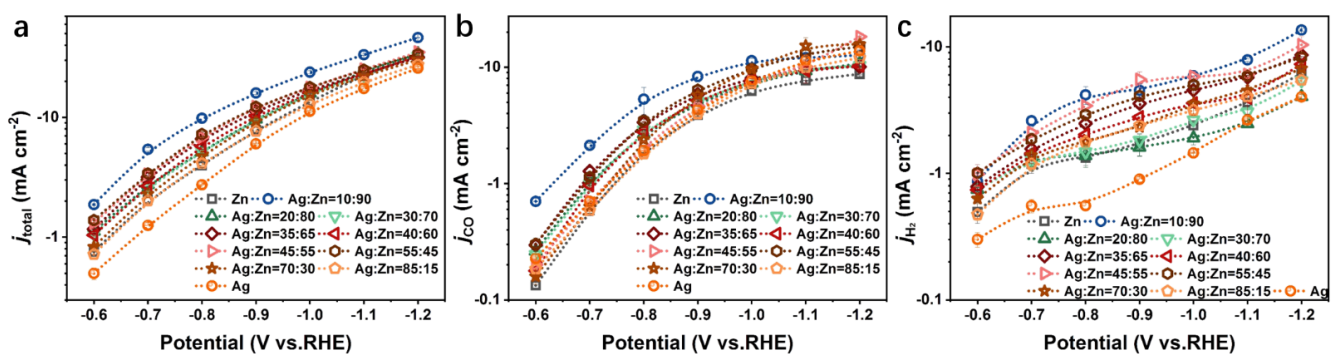


Figure 5. (a) j_{total} , (b) j_{CO} , and (c) j_{H_2} for the pure Zn, pure Ag, and Ag-Zn alloy catalysts with different element concentrations.

The partial current density towards specific CO₂RR products is another important figure of merit which is useful in comparing CO₂RR catalysts. Because the partial current density is directly proportional to the turnover frequency (TOF) of a certain product, the presentation of the data is useful in obtaining insights into the kinetics and mechanisms of the reduction reactions [18]. The partial current densities of CO (j_{CO}) and H₂ (j_{H_2}) are presented in Figure 5b,c in the form of a semi-log Tafel plot, respectively. The observed trend of j_{CO} is similar for all catalysts (Figures 5b and S9). In the less negative potential region, the TOF of CO formation increases with the decrease of potentials, whereas in the region of lower potentials, this growth of TOF gradually slows down and reaches a plateau, which is assigned to a CO₂-mass-transport limitation in aqueous solution due to its low solubility at atmospheric pressure [31,38], consistent with FE_{CO} in Figure 4a. To obtain further insights into these catalysts, their Tafel plots were investigated and presented in Figure S10. A small Tafel slope is beneficial in practical applications because it will lead to a much faster increase in the increment of CO₂ reduction rate with increasing overpotential [13]. For the catalysts with the Ag/Ag(Zn) solid solution phase, j_{CO} increases as a function of overpotential with a slope of 233, 221, 188, and 187 mV dec⁻¹ for the Ag, Ag₈₅Zn₁₅, Ag₇₀Zn₃₀, and Ag₅₅Zn₄₅ catalysts, respectively in the lower overpotential region (Figure S10a). It is observed that the Tafel slope decreases gradually with a higher Zn content, and when the Ag-Zn alloy behaves as the AgZn phase, the Ag₄₀Zn₆₀ catalyst shows the lowest Tafel slope which is only 165 mV dec⁻¹ (Figure S10b). While for the Ag₅Zn₈ and AgZn₃ phase catalysts, the Tafel slope is even larger than that of the pure Zn (Figure S10c). These results indicate that the alloying of Ag with Zn can improve the reaction kinetics of CO₂RR, and the enhanced degree depends on the phase composition and element concentration.

As shown in Figure 5c, j_{H_2} of the catalysts with different phase compositions forms transient platforms in different potential regions. The platform of pure Ag and AgZn phase catalysts appears between -0.7~-0.8 V and -0.9~-1.1 V vs. RHE, respectively (Figure S11a,b), and that of Ag₅Zn₈, AgZn₃ and Zn phase catalysts appears between -0.7~-0.9 V vs. RHE (Figure S11c). This reflects the observed shift in selectivity from hydrogen to CO in this platform region, as discussed earlier [18]. In the more negative potential region, an increase in the TOF of H₂ is observed, which explains the slight rebound of H₂ and the production of other products in this potential region.

4. Conclusions

In summary, a series of Ag-Zn thin alloy film catalysts with different concentrations were prepared by a simple co-sputtering method, and the effect of different element concentrations and phase compositions on the activity and selectivity of CO₂RR was analyzed. It can be seen from the results that different phase compositions have affected the trend of FE_{CO} and the selectivity from hydrogen to CO with varying potentials. Pure Ag catalyst exhibits the best CO₂ selectivity, and the alloying with Zn does not significantly increase the activity of CO₂RR for the Ag/Ag(Zn) phase catalysts. The Ag₅Zn₈ and AgZn₃ phase catalysts show higher CO selectivity than pure Zn due to the synergistic effect of the Ag-Zn alloy. The alloying of Ag with Zn could improve the activity of the catalysts and the reaction kinetics of CO₂RR, and the AgZn₃ phase catalyst has the highest activity. The present work could provide guidelines for the design of Ag-Zn alloy catalysts for efficient CO₂RR.

Supplementary Materials: The following are available online at <https://www.mdpi.com/article/10.3390/ma15196892/s1>, Figure S1: Typical EDX spectra of (a) Ag₁₀Zn₉₀, (b) Ag₂₀Zn₈₀, (c) Ag₃₀Zn₇₀, (d) Ag₃₅Zn₆₅, (e) Ag₄₀Zn₆₀, (f) Ag₄₅Zn₅₅, (g) Ag₅₅Zn₄₅, (h) Ag₇₀Zn₃₀ and (i) Ag₈₅Zn₁₅ films, Figure S2: Macroscopic view of the (a) Zn film and (b) Ag film, Figure S3: SEM images of (a) Ag₁₀Zn₉₀, (b) Ag₂₀Zn₈₀, (c) Ag₃₀Zn₇₀, (d) Ag₃₅Zn₆₅, (e) Ag₄₀Zn₆₀, (f) Ag₄₅Zn₅₅, (g) Ag₅₅Zn₄₅, (h) Ag₇₀Zn₃₀ and (i) Ag₈₅Zn₁₅ films, Figure S4: XRD pattern of the CFP, Figure S5: FE_{CO} for the (a) Ag, Ag(Zn), (b) AgZn, (c) Ag₅Zn₈, AgZn₃, and Zn phase catalysts, Figure S6: FE_{H₂} for the (a) Ag, Ag(Zn), (b) AgZn, (c) Ag₅Zn₈, AgZn₃, and Zn phase catalysts, Figure S7: FE_{CO&H₂} for the (a) Ag, Ag(Zn),

(b) AgZn, (c) Ag₅Zn₈, AgZn₃, and Zn phase catalysts, Figure S8: j_{total} for the (a) Ag, Ag(Zn), (b) AgZn, (c) Ag₅Zn₈, AgZn₃, and Zn phase catalysts, Figure S9: j_{CO} for the (a) Ag, Ag(Zn), (b) AgZn, (c) Ag₅Zn₈, AgZn₃, and Zn phase catalysts, Figure S10: Tafel plots of the (a) Ag, Ag(Zn), (b) AgZn, (c) Ag₅Zn₈, AgZn₃ and Zn phase catalysts, Figure S11: j_{H_2} for the (a) Ag, Ag(Zn), (b) AgZn, (c) Ag₅Zn₈, AgZn₃, and Zn phase catalysts.

Author Contributions: Conceptualization, J.S.; methodology, J.S., B.Y., X.Y., F.T., J.W. and W.Y.; formal analysis, J.S., B.Y., X.Y., F.T., J.W. and W.Y.; investigation, J.S., B.Y., X.Y., F.T., J.W. and W.Y.; writing—original draft preparation, J.S.; writing—review and editing, J.S., G.C. and Z.Z.; supervision, Z.Z., G.C. and W.Y.; project administration, Z.Z.; funding acquisition, Z.Z. and G.C. All authors have read and agreed to the published version of the manuscript.

Funding: The authors gratefully acknowledge the financial support from the Natural Science Foundation of Shandong Province (ZR2021QE229), the National Natural Science Foundation of China (51871133), China Postdoctoral Science foundation (2022M710077), Taishan Scholar Foundation of Shandong Province, and the Key Research and Development Program of Shandong Province (2021ZLGX01).

Institutional Review Board Statement: Not applicable.

Informed Consent Statement: Not applicable.

Data Availability Statement: All data are available within the paper and its Supplementary Information files or from the corresponding authors upon request.

Conflicts of Interest: The authors declare no conflict of interest.

References

1. Turner, J.A. A Realizable Renewable Energy Future. *Science* **1999**, *285*, 687–689. [[CrossRef](#)] [[PubMed](#)]
2. Spinner, N.S.; Vega, J.A.; Mustain, W.E. Recent Progress in the Electrochemical Conversion and Utilization of CO₂. *Catal. Sci. Technol.* **2012**, *2*, 19–28. [[CrossRef](#)]
3. Peter, S.C. Reduction of CO₂ to Chemicals and Fuels: A Solution to Global Warming and Energy Crisis. *ACS Energy Lett.* **2018**, *3*, 1557–1561. [[CrossRef](#)]
4. Tu, W.G.; Zhou, Y.; Zou, Z.G. Photocatalytic Conversion of CO₂ into Renewable Hydrocarbon Fuels: State-of-the-Art Accomplishment, Challenges, and Prospects. *Adv. Mater.* **2014**, *26*, 4607–4626. [[PubMed](#)]
5. Lahijani, P.; Zainal, Z.A.; Mohammadi, M.; Mohamed, A.R. Conversion of the Greenhouse Gas CO₂ to the Fuel Gas CO via the Boudouard Reaction: A Review. *Renew. Sustain. Energy Rev.* **2015**, *41*, 615–632.
6. Gonzales, J.N.; Matson, M.M.; Atsumi, S. Nonphotosynthetic Biological CO₂ Reduction. *Biochemistry* **2019**, *58*, 1470–1477. [[CrossRef](#)] [[PubMed](#)]
7. Hirunsit, P.; Soodsawang, W.; Limtrakul, J. CO₂ Electrochemical Reduction to Methane and Methanol on Copper-Based Alloys: Theoretical insight. *J. Phys. Chem. C* **2015**, *119*, 8238–8249. [[CrossRef](#)]
8. Lee, S.M.; Lee, H.; Kim, J.; Ahn, S.H.; Chang, S.T. All-Water-Based Solution Processed Ag Nanofilms for Highly Efficient Electrocatalytic Reduction of CO₂ to CO. *Appl. Catal. B Environ.* **2019**, *259*, 118045. [[CrossRef](#)]
9. Ramdin, M.; Morrison, A.R.T.; de Groen, M.; van Haperen, R.; de Kler, R.; van den Broeke, L.J.P.; Trusler, J.P.M.; de Jong, W.; Vlugt, T.J.H. High Pressure Electrochemical Reduction of CO₂ to Formic Acid/Formate: A Comparison Between Bipolar Membranes and Cation Exchange Membranes. *Ind. Eng. Chem. Res.* **2019**, *58*, 1834–1847. [[CrossRef](#)]
10. Centi, G.; Quadrelli, E.A.; Perathoner, S. Catalysis for CO₂ Conversion: A Key Technology for Rapid Introduction of Renewable Energy in the Value Chain of Chemical Industries. *Energy Environ. Sci.* **2013**, *6*, 1711–1731. [[CrossRef](#)]
11. Gao, Y.; Li, F.; Zhou, P.; Wang, Z.; Zheng, Z.; Wang, P.; Liu, Y.; Dai, Y.; Whangbo, M.-H.; Huang, B. Enhanced Selectivity and Activity for Electrocatalytic Reduction of CO₂ to CO on an Anodized Zn/Carbon/Ag Electrode. *J. Mater. Chem. A* **2019**, *7*, 16685–16689. [[CrossRef](#)]
12. Jo, A.; Kim, S.; Park, H.; Park, H.-Y.; Jang, J.H.; Park, H.S. Enhanced Electrochemical Conversion of CO₂ to CO at Bimetallic Ag-Zn Catalysts Formed on Polypyrrole-Coated Electrode. *J. Catal.* **2021**, *393*, 92–99. [[CrossRef](#)]
13. Liu, K.; Wang, J.; Shi, M.; Yan, J.; Jiang, Q. Simultaneous Achieving of High Faradaic Efficiency and CO Partial Current Density for CO₂ Reduction via Robust, Noble-Metal-Free Zn Nanosheets with Favorable Adsorption Energy. *Adv. Energy Mater.* **2019**, *9*, 1900276. [[CrossRef](#)]
14. Lu, Q.; Rosen, J.; Jiao, F. Nanostructured Metallic Electrocatalysts for Carbon Dioxide Reduction. *Chemcatchem* **2015**, *7*, 38–47. [[CrossRef](#)]
15. Hori, Y.; Wakebe, H.; Tsukamoto, T.; Koga, O. Electrocatalytic Process of CO Selectivity in Electrochemical Reduction of CO₂ at Metal-Electrodes in Aqueous-Media. *Electrochim. Acta.* **1994**, *39*, 1833–1839. [[CrossRef](#)]

16. Jones, J.P.; Prakash, G.K.S.; Olah, G.A. Electrochemical CO₂ Reduction: Recent Advances and Current Trends. *Isr. J. Chem.* **2014**, *54*, 1451–1466. [[CrossRef](#)]
17. Peterson, A.A.; Nørskov, J.K. Activity descriptors for CO₂ Electroreduction to Methane on Transition-Metal Catalysts. *J. Phys. Chem. Lett.* **2012**, *3*, 251–258. [[CrossRef](#)]
18. Hatsukade, T.; Kuhl, K.P.; Cave, E.R.; Abram, D.N.; Jaramillo, T.F. Insights into the Electrocatalytic Reduction of CO₂ on Metallic Silver Surfaces. *Phys. Chem. Chem. Phys.* **2014**, *16*, 13814–13819. [[CrossRef](#)]
19. Lee, C.Y.; Zhao, Y.; Wang, C.Y.; Mitchell, D.R.G.; Wallace, G.G. Rapid Formation of Self-Organised Ag Nanosheets with High Efficiency and Selectivity in CO₂ Electroreduction to CO. *Sustain. Energy Fuels* **2017**, *1*, 1023–1027. [[CrossRef](#)]
20. Zhong, H.X.; Ghorbani-Asl, M.; Ly, K.H.; Zhang, J.C.; Ge, J.; Wang, M.C.; Liao, Z.Q.; Makarov, D.; Zschech, E.; Brunner, E.; et al. Synergistic Electroreduction of Carbon Dioxide to Carbon Monoxide on Bimetallic Layered Conjugated Metal-Organic Frameworks. *Nat. Commun.* **2020**, *11*, 1409. [[CrossRef](#)]
21. Feaster, J.T.; Shi, C.; Cave, E.R.; Hatsukade, T.; Abram, D.N.; Kuhl, K.P.; Hahn, C.; Nørskov, J.K.; Jaramillo, T.F. Understanding Selectivity for the Electrochemical Reduction of Carbon Dioxide to Formic Acid and Carbon Monoxide on Metal Electrodes. *ACS Catal.* **2017**, *7*, 4822–4827. [[CrossRef](#)]
22. Hitt, J.L.; Li, Y.C.; Tao, S.; Yan, Z.; Gao, Y.; Billinge, S.J.L.; Mallouk, T.E. A High Throughput Optical Method for Studying Compositional Effects in Electrocatalysts for CO₂ Reduction. *Nat. Commun.* **2021**, *12*, 1114. [[CrossRef](#)]
23. Gerken, J.B.; Shaner, S.E.; Masse, R.C.; Porubsky, N.J.; Stahl, S.S. A Survey of Diverse Earth Abundant Oxygen Evolution Electrocatalysts Showing Enhanced Activity from Ni-Fe Oxides Containing a Third Metal. *Energy Environ. Sci.* **2014**, *7*, 2376–2382. [[CrossRef](#)]
24. Sun, J.M.; Yu, B.; Tan, F.Q.; Yang, W.F.; Cheng, G.H.; Zhang, Z.H. High Throughput Preparation of Ni-Mo alloy Thin Films as Efficient Bifunctional Electrocatalysts for Water Splitting. *Int. J. Hydrogen Energy* **2022**, *47*, 15764–15774. [[CrossRef](#)]
25. Gao, H.; Yan, X.J.; Niu, J.Z.; Zhang, Y.; Song, M.J.; Shi, Y.J.; Ma, W.S.; Qin, J.Y.; Zhang, Z.H. Scalable Structural Refining via Altering Working Pressure and In-situ Electrochemically-Driven Cu-Sb Alloying of Magnetron Sputtered Sb Anode in Sodium Ion Batteries. *Chem. Eng. J.* **2020**, *388*, 124299. [[CrossRef](#)]
26. Liu, N.; Yin, K.; Si, C.; Kou, T.; Zhang, Y.; Ma, W.; Zhang, Z. Hierarchically Porous Nickel-Iridium-Ruthenium-Aluminum Alloys with Tunable Compositions and Electrocatalytic Activities towards the Oxygen/Hydrogen Evolution Reaction in Acid Electrolyte. *J. Mater. Chem. A* **2020**, *8*, 6245–6255. [[CrossRef](#)]
27. Lamaison, S.; Wakerley, D.; Kracke, F.; Moore, T.; Zhou, L.; Lee, D.U.; Wang, L.; Hubert, M.A.; Aviles Acosta, J.E.; Gregoire, J.M.; et al. Designing a Zn-Ag Catalyst Matrix and Electrolyzer System for CO₂ Conversion to CO and Beyond. *Adv. Mater.* **2022**, *34*, 2103963. [[CrossRef](#)]
28. Hansen, H.A.; Varley, J.B.; Peterson, A.A.; Nørskov, J.K. Understanding Trends in the Electrocatalytic Activity of Metals and Enzymes for CO₂ Reduction to CO. *J. Phys. Chem. Lett.* **2013**, *4*, 388–392. [[CrossRef](#)]
29. Hori, Y. CO₂ Reduction Using Electrochemical Approach. In *Solar to Chemical Energy Conversion*, 1st ed.; Springer: New York, NY, USA, 2016; pp. 191–211.
30. Kuhl, K.P.; Hatsukade, T.; Cave, E.R.; Abram, D.N.; Kibsgaard, J.; Jaramillo, T.F. Electrocatalytic Conversion of Carbon Dioxide to Methane and Methanol on Transition Metal Surfaces. *J. Am. Chem. Soc.* **2014**, *136*, 14107–14113. [[CrossRef](#)]
31. Hatsukade, T.; Kuhl, K.P.; Cave, E.R.; Abram, D.N.; Feaster, J.T.; Jongnerius, A.L.; Hahn, C.; Jaramillo, T.F. Carbon Dioxide Electroreduction Using a Silver-Zinc Alloy. *Energy Technol.* **2017**, *5*, 955–961. [[CrossRef](#)]
32. Giamello, E.G.; Fubini, B. Heat of Adsorption of Carbon Monoxide on Zinc Oxide Pretreated by Various Methods. *J. Chem. Soc. Faraday Trans. 1* **1983**, *79*, 1995–2003. [[CrossRef](#)]
33. Park, S.A.; Lim, H.; Kim, Y.T. Enhanced Oxygen Reduction Reaction Activity Due to Electronic Effects Between Ag and Mn₃O₄ in Alkaline Media. *ACS Catal.* **2015**, *5*, 3995–4002. [[CrossRef](#)]
34. Tang, W.; Huang, D.L.; Wu, L.L.; Zhao, C.Z.; Xu, L.L.; Gao, H.; Zhang, X.T.; Wang, W.B. Surface Plasmon Enhanced Ultraviolet emission and Observation of Random Lasing from Self-Assembly Zn/ZnO Composite Nanowires. *Crystengcomm* **2011**, *13*, 2336–2339. [[CrossRef](#)]
35. Zhao, Z.; Lu, G. Computational Screening of Near-Surface Alloys for CO₂ Electroreduction. *ACS Catal.* **2018**, *8*, 3885–3894. [[CrossRef](#)]
36. Guo, W.; Shim, K.; Kim, Y.-T. Ag Layer Deposited on Zn by Physical Vapor Deposition with Enhanced CO Selectivity for Electrochemical CO₂ Reduction. *Appl. Surf. Sci.* **2020**, *526*, 146651. [[CrossRef](#)]
37. Zhang, Z.; Wen, G.; Luo, D.; Ren, B.; Zhu, Y.; Gao, R.; Dou, H.; Sun, G.; Feng, M.; Bai, Z.; et al. “Two Ships in a Bottle” Design for Zn-Ag-O Catalyst Enabling Selective and Long-Lasting CO₂ Electroreduction. *J. Am. Chem. Soc.* **2021**, *143*, 6855–6864. [[CrossRef](#)]
38. Lamaison, S.; Wakerley, D.; Blanchard, J.; Montero, D.; Rousse, G.; Mercier, D.; Marcus, P.; Taverna, D.; Giaume, D.; Mougél, V.; et al. High-Current-Density CO₂-to-CO Electroreduction on Ag-Alloyed Zn Dendrites at Elevated Pressure. *Joule* **2020**, *4*, 395–406. [[CrossRef](#)]